ACS Catalysis

pubs.acs.org/acscatalysis

Research Article

Enhanced ORR Kinetics on Au-Doped Pt−Cu Porous Films in Alkaline Media

Yunxiang Xie, Yao Yang, David A. Muller, Héctor D. Abruña, Nikolay Dimitrov,* and Jiye Fang*

Cite This: *ACS Catal.* 2020, 10, 9967−9976

Read Online

ACCESS | Metrics & More | Article Recommendations | Supporting Information

ABSTRACT: Fraction-controlled Pt−Cu-based porous films were prepared using an electrochemical deposition−stripping synthetic approach, and their structure, composition, and electronic structure were characterized using scanning/transmission electron microscopy-energy dispersive X-ray spectroscopy, and X-ray photoelectron spectroscopy techniques. These materials exhibited superb electrocatalytic activity toward the oxygen reduction reaction (ORR) in alkaline media. For example, the mass activity of a $Pt_{45}Cu_{55}$ film, at 0.90 V (vs RHE), was 3.5× higher than that of commercial Pt/C (40 wt % Pt). This activity enhancement is attributed, in part, to the ligand effect of the Cu component. The introduction of Au, as a third metal constituent to the porous films, further improved the ORR performance significantly. The synergistic effect(s) of Au and Pt appear to have a critical impact on the enhancement of the ORR activity. Compositional optimization identified the dealloyed $Pt_{37}Cu_{56}Au_7$ porous film as the best performing electrocatalyst. It also exhibited the highest mass and specific activities (0.871 A/mg_{Pt}, 1.85 mA/cm^2) which were 7.20× and 8.15× higher than those of commercial Pt/C (40 wt % Pt), respectively. This ternary alloy thin-film catalyst also exhibited the longest durability, among all tested samples in this study.

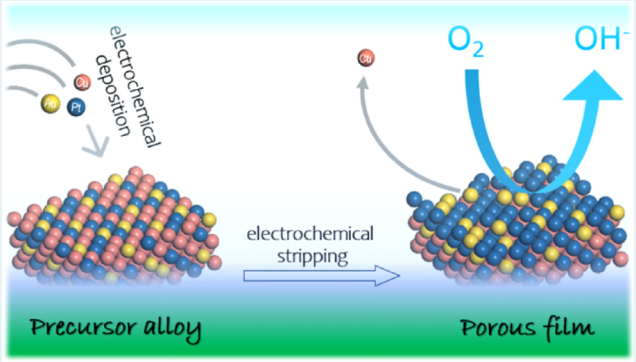

KEYWORDS: *electrochemical deposition, dealloying, porous film, electrocatalysis, ORR, alkaline media*

1. INTRODUCTION

Alkaline fuel cells (AFCs) which could achieve power generation efficiencies of up to 70%[1] were used as power sources among the first-developed fuel cells in the space program.[2] These AFCs employed a liquid solution of potassium hydroxide (KOH) as the electrolyte that conducted ions between the anode and cathode.[1] Unlike the acidic environment of polymer-electrolyte membrane fuel cells, the alkaline media in AFCs could provide a less corrosive environment[3] for protecting the electrocatalysts and relatively fast kinetics[4] for the oxygen reduction reaction (ORR). However, they were also prone to severe performance degradation due to carbonation effects arising from the presence of mobile cations.

The ORR is one of the most important reactions in fuel cells as most alternative cathode reactions are not practical. Even though the alkaline environment favors the ORR,[4] it is still sluggish, requiring high overpotentials (>300 mV). This limits the efficiency and power output of AFCs.[5] Extensive efforts have been dedicated to the improvement of ORR activities in alkaline media. Many monometallic catalysts [gold (Au),[6] platinum (Pt),[6] silver (Ag),[7] palladium (Pd),[8] etc.] have been studied. Among these, Au(100) possesses a particularly high ORR activity that is comparable to that of Pt(111) in alkaline media.[9,10] Further developments have pursued optimization of the Pt electronic structure (d-band center) by introducing first-row transition metals, such as copper (Cu)[11,12] and nickel (Ni),[13] as alloying elements. This is believed to be another effective way to both enhance the catalytic activity and lower the cost of the electrocatalysts. By alloying Pt with transition metals, the strain effect[14] associated with the change of the Pt lattice parameter and the ligand effect,[15] induced by the interaction between Pt and the other transition metal(s), enabled the deliberate tuning of the d-band center of the resultant alloy. This, in turn, could impact the *OH binding energy (BE) that is of key importance for improving the ORR kinetics.[4,11]

Previous ORR studies on Pt(111) with subsurface Cu,[11] as well as on plain Au(100) single crystals,[9] demonstrated a Sabatier volcano relationship in alkaline media for both the ORR activity and the BE of *OH. Inspired by these results

Received: June 18, 2020
Revised: July 31, 2020
Published: August 7, 2020

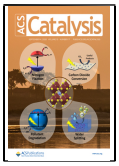

https://dx.doi.org/10.1021/acscatal.0c02690
ACS Catal. 2020, 10, 9967−9976

aimed at boosting ORR performance in alkaline media, researchers investigated PtAuCu@Cu_2O/Pt nanobranch structures,[16] PtAu super-lattices,[17] and PtCu nanocubic frames.[18] However, the ORR performance of these Au alloy-based catalysts was disappointing likely because of the high Au contents in the above catalysts that are believed to upshift the Pt d-band center, resulting in an increase in the *OH BE and, consequently, lowering the electrocatalytic activity.[19,20] In addition, a previous study indicated that a Pt surface with Cu underneath represented a promising target in the process of catalyst design to boost ORR performance.[11] Therefore, there is still an outstanding need for the rational design of electrocatalysts to improve the ORR catalytic performance in alkaline media.

Recent reports indicate that it would be desirable to synthesize ORR catalysts with a Cu-core and Pt-shell structure along with the introduction of trace amounts of Au as a surface dopant. Previous studies indicated that Pt−Cu−Au thin films, fabricated via electrodeposition followed by a dealloying process, enabled a controllable composition with a unique interpenetrating solid-void structure where the solid phase, represented by "snaky" ligaments, consisted of a noble-metal-rich surface and a less noble-metal-dominated core. Such structures feature very high surface areas, compared to traditional nanoparticles.[21−24]

Herein, we report on the development and optimization of composition-controlled Pt−Cu−Au thin films using a facile electrodeposition−stripping method and present comprehensive testing of these films as ORR electrocatalysts, for high activity and long term durability toward the ORR in alkaline media. Scanning electron microscopy (SEM) and energy dispersive X-ray spectroscopy (EDX) were used for morphological and compositional analyses, and scanning transmission electron microscopy (STEM)/EDX was employed for mapping core/surface elemental distributions. The electronic structure of these thin-film catalysts was probed by X-ray photoelectron spectroscopy (XPS), and the electrochemical surface area (ECSA) comprising Pt active sites and the Pt electronic structure were characterized by hydrogen UPD (H UPD) and CO striping techniques, respectively. Linear sweep voltammetry (LSV) and cyclic voltammetry (CV) were employed for ORR activity and durability tests.

2. EXPERIMENTAL SECTION

2.1. Electrode Preparation. Au and Pt rotating-disk-electrodes (RDEs) (Pine Instruments) with a 5.0 mm diameter were used as working electrodes (WEs) for electrochemical characterization and measurements. All WEs were first mechanically polished using 1 μm alumina slurry (Buehler) followed by rinsing with Barnstead Nanopure water (18.2 MΩ cm). The WE was then immersed in a warm solution containing concentrated HNO_3 to remove trace contaminants followed by rinsing with Barnstead Nanopure water. The Au RDE was used as a catalyst (Pt−Cu−Au or Pt−Cu porous films) carrier. The Pt RDE was used for a further comparative mechanistic investigation. Finally, glassy carbon WEs, subjected to the same preparation routines employed for the Au RDE, were used as the carriers of electrocatalysts for the SEM and EDX characterizations.

2.2. Catalyst Preparation. The deposition of Pt−Cu−Au and Pt−Cu on the Au RDE surface was achieved by overpotential codeposition in a three-electrode cell at −0.70 V versus a saturated mercury-mercurous sulfate electrode (MSE) used as a reference electrode (RE). A Pt wire was used as the counter electrode for all the electrochemical experiments. The deposition solution for Pt−Cu−Au alloys contained 0.80 mM $Cu(ClO_4)_2$ (Alfa Aesar, 99.999%), 0.18 mM K_2PtCl_4 (GFS Chemical, 98%), 0.03 mM or 0.18 mM $NaAuCl_4{\cdot}2H_2O$ (PREMION, 99.99%), 50 mM HCl (J.T. Baker, 36.5−38.0%), and 100 mM $NaClO_4$ (GFS Chemicals, 98%). The deposition solution for Pt−Cu alloys was the same as that described above but in the absence of $NaAuCl_4{\cdot}2H_2O$. An Au-cluster-decorated Pt RDE was prepared through pulse deposition for 1 s at −0.55 V versus MSE in a solution containing 0.5 mM $NaAuCl_4$ $2H_2O$, 10 mM $HClO_4$ (GFS Chemical, 70% distilled), and 100 mM $NaClO_4$.[25] All the solutions were purged with ultrahigh purity N_2 for at least 30 min before use. The total mass of the deposited alloys was controlled by the total deposition charge which was fixed at 50 mC/cm^2. The mass of Pt was calculated by multiplying the total deposition charge by the Pt atomic fraction determined by EDX. After the deposition, the resultant alloy film, designated as the "precursor alloy", was rinsed thoroughly with Barnstead Nanopure water and then dried gently with ultrapure N_2. Anodic LSV was used to monitor the dealloying routine for the selective removal of Cu from the as-deposited Pt−Cu or Pt−Cu−Au precursor alloy. These experiments were carried out in a solution containing 1 mM $CuSO_4$ (J.T. Baker, 99.8%) and 100 mM $HClO_4$. A Cu wire was used as the pseudo-RE [0.25 V vs standard hydrogen electrode (SHE)] in the dealloying experiments. The dealloying protocol consisted of anodic potential scans from 0.10 to 1.25 V versus Cu/Cu^{2+} at a scan rate of 1 mV s^{-1}, generating composition-controlled electrocatalyst films, denoted as the "porous film". A PAR model 273 Potentiostat/Galvanostat operated by a PC equipped with Corrware software was used for the overpotential codeposition, anodic LSV, and pulse deposition experiments. Pt nanoparticulate catalysts, supported on carbon black, were used for comparative catalytic testing (Alfa Aesar, HisPECTM 4000, 40 wt % Pt). The Pt nanoparticle ink was prepared by mixing 1.0 mg of Pt/C (40 wt % Pt) with 0.50 mL of 1-propanol, 0.50 mL of Barnstead Nanopure water, and 0.04 mL of Nafion (Sigma-Aldrich, 5 wt %). Then, 10 μL of 1 mg/mL Pt/C (40 wt % Pt) nanoparticle ink was drop-cast on the Au RDE for ORR tests.

2.3. Structural and Compositional Characterization. SEM (Zeiss Supra 55 VP) coupled with an in-lens and SE2 detector, operated at an accelerating voltage from 5 to 15 keV, was employed for the structural characterization of the porous films using a working distance between 3 and 6 mm. The elemental composition of the synthesized Pt−Cu−Au and Pt−Cu porous films was determined by EDX equipped in SEM and operated at an accelerating voltage of 15 kV and a working distance of 8.5 mm. STEM mapping was conducted on an FEI Tecnai F20 at 200 keV with a screen current of ∼3 nA. XPS analysis was carried out on a PHI 500 VersaProbe XPS. A scanned and focused monochromatic Al Kα X-ray beam was utilized to irradiate elements on the sample surface. The emitted photoelectrons were captured and analyzed by a hemispherical analyzer with 16 channels. The electronic structure was analyzed using the BE position. STEM and EDX results were collected in an FEI Tecnai F-20 electron microscope equipped with an Oxford X-Max detector.

2.4. Surface Characterization. The ECSA of Pt was estimated by CV scanning at 50 mV s^{-1} in a 0.5 M H_2SO_4 (GFS Chemical, redistilled 95−98%) solution over the

https://dx.doi.org/10.1021/acscatal.0c02690
ACS Catal. 2020, 10, 9967−9976

potential range between −0.65 and 0.45 V versus the MSE [reported vs reversible hydrogen electrode (RHE) after conversion by adding 0.65 V]. We employed a Pine Instruments model AFCBP Bipontentiostat interfaced with a PC through Aftermath Data Organizer software. All solutions were purged using ultrahigh purity N_2 for at least 30 min before use. The ECSA of Pt was calculated by integrating the area of H UPD over the potential range from 0.00 to 0.25 V (vs RHE). For H UPD, the following equation was used to calculate the ECSA of Pt[26,27] ($A_{\text{Pt-H UPD}} = Q_{\text{H UPD}}$ (μC)/210 μC cm^{-2}). The CO stripping technique was used to confirm the ECSA of Pt, comparatively with the H UPD method, and to also probe the electronic structure of Pt. The as-prepared catalysts were immersed into a solution containing 0.5 M H_2SO_4, and then, the solution was purged for 10 min with CO gas while a potential of −0.160 V versus the Ag/AgCl (sat'd KCl) RE was applied. Next, the solution was purged with ultrahigh purity N_2 for 20 min to eliminate CO in the solution. Finally, a CV scan from −0.20 to 1.00 V versus the Ag/AgCl (sat'd KCl) RE (presented vs the RHE after conversion by adding 0.20 V) at 50 mV s^{-1} was applied to strip the adsorbed CO. Another cycle was applied after the first stripping cycle to ensure the complete removal of the CO adlayer from the surface. For CO stripping, the following equation was used to calculate the ECSA of Pt[28,29] ($A_{\text{Pt-CO stripping}} = Q_{\text{CO Stripping}}(\mu\text{C})/420\ \mu\text{C cm}^{-2}$).

The ECSA was evaluated by considering the Pt area determined by the CO stripping method and the overall Pt loading. A Gamry Interface 1000 Potentiostat/Galvanostat/ZRA operated by a PC equipped with Gamry framework was used for controlling the CO stripping test. The Pt area was calculated by integrating the area of the CO stripping curve.

2.5. ORR Studies. A Gamry Interface 1000 Potentiostat/Galvanostat/ZRA connected to a Gamry RDE710 operated by a PC equipped with a Gamry framework was used for ORR tests. The experiments were conducted in a conventional three-electrode cell with Ag/AgCl (sat'd KCl) as the RE. The Ag/AgCl RE has a potential of 0.200 V versus the SHE. The potential value was normalized to the RHE as indicated in eq 1.

$$E(\text{V, RHE}) = E(\text{V vs Ag/AgCl}) + 0.0592\text{pH} + 0.200\ \text{V} + (iR) \quad (1)$$

The ORR performance was evaluated by anodic LSV with a catalyst-loaded RDE at a scan rate of 10 mV/s and a rotation rate of 1,600 rpm in oxygen (O_2)-saturated 0.1 M KOH. The kinetic current (j_k) was calculated by using the Koutecky–Levich (K–L) equation.[30]

$$1/j = 1/j_k + 1/j_d \quad (2)$$

The number of transferred electrons was calculated by using the Levich equation[30] (eq 3).

$$j_d = 0.2nF(D_{O_2})^{2/3}\nu^{-1/6}\omega^{1/2}CO_2 \quad (3)$$

Here, n is the number of electrons transferred per O_2, F is the Faraday constant (96,485 C/mol), D_{O_2} is the diffusion coefficient of O_2 in the electrolyte (1.9×10^{-5} cm^2/s), ν is the kinetic viscosity of 0.1 M KOH (0.01 cm^2/s), ω is the rotation speed in rpm, and C_{O2} is the concentration of O_2 in 0.1 M KOH (1.2×10^{-6} mol/cm^3).[31] An accelerated durability test (ADT) was performed between 0.6 and 1.0 V (vs RHE) at a scan rate of 100 mV/s for up to 10,000 cycles. *iR* compensation was applied to the ORR measurements to enable a comparison of electrocatalytic activity. A resistance of 40 Ω, determined from the high-frequency impedance, was assumed to remain constant during the measurements.

3. RESULTS AND DISCUSSION

3.1. Characterization of the Prepared Catalysts. *3.1.1. Alloy Structure and Morphology.* The ternary Pt–Cu–Au porous films were successfully prepared by the facile electrochemical synthesis. Figure 1a,c displays the structure of

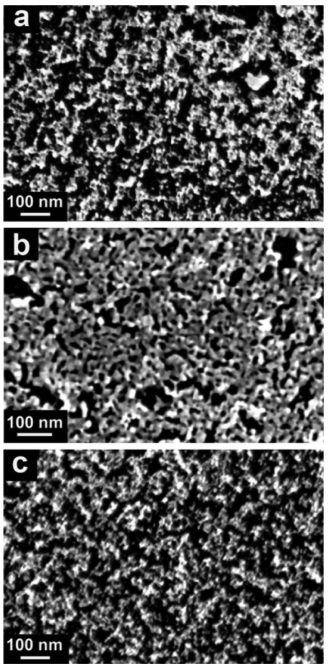

Figure 1. SEM images of porous films with different compositions (a) $Pt_{37}Cu_{56}Au_7$; (b) $Pt_{23}Cu_{52}Au_{25}$; and (c) $Pt_{45}Cu_{55}$.

the $Pt_{37}Cu_{56}Au_7$ and $Pt_{45}Cu_{55}$ porous films, respectively. Figure S1 presents the morphology of the as-deposited (before dealloying) $Pt_{15}Cu_{82}Au_3$ film which appears as resulting from deposition by dense nucleation. A first glance analysis on the light and dark regions (pores and ligaments respectively) in the SEM micrographs presented in Figure 1a,c suggests that the overall morphology is a porous structure with a ligament size of 20–30 nm. Figure 1b presents an SEM image of the $Pt_{23}Cu_{52}Au_{25}$ porous film. It is seen that the ligaments become finer with an increase of the Pt content (Figure 1a,c). This phenomenon has been attributed to the low mobility of Pt.[22] STEM–EDX elemental maps showed the elemental analysis of $Pt_{37}Cu_{56}Au_7$ at the nanometer scale (Figure 2), which was based on the Pt Lα, Au Lα, and Cu Kβ edges in the EDX spectrum (Figure S2). Composite maps of Pt/Au and Pt/Cu showed a relatively homogenous distribution of Pt, Au, and Cu in these ternary alloys (Figure 2b,c). Quantitative EDX analysis showed an average composition of 37.8 ± 1.4 at. % Pt, 52.6 ± 2.2 at. % Cu, and 9.6 ± 2.5 at. % Au (Table S1), which is consistent with the chemical formula, $Pt_{37}Cu_{56}Au_7$.

3.1.2. Alloy Composition and Electronic Structure. The compositions of the precursor alloys and dealloyed porous films were determined using SEM–EDX analysis (Figure S3). The details of the component analysis are summarized in Table

https://dx.doi.org/10.1021/acscatal.0c02690
ACS Catal. 2020, 10, 9967–9976

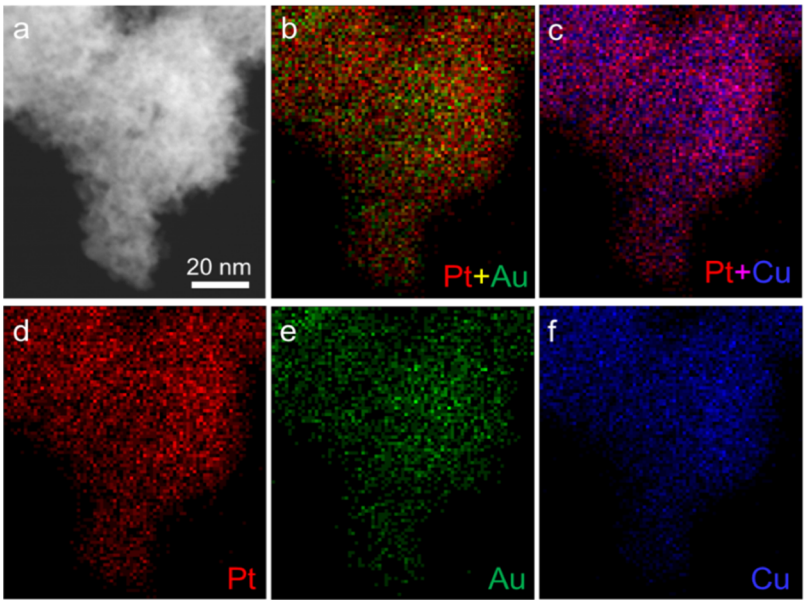

Figure 2. (a) HAADF-STEM image of the $Pt_{37}Cu_{56}Au_7$ porous film and the corresponding EDX elemental maps of Pt in red (d), Au in green (e), Cu in blue (f), and composite maps of Pt vs Au (b) and Pt vs Cu (c), showing relatively homogenous distributions.

Table 1. EDX Results of the Prepared Thin-Film Catalysts (Molar Ratios)

sample inputs (elemental ratio in the input solution for deposition, Pt/Cu/Au)	precursor compositions determined by EDX (Pt/Cu/Au)	compositions of porous films (de-alloyed) determined by SEM−EDX (Pt/Cu/Au)
18:82	18:82	45.7:54.3
18:80.5:1.5	15:83.5:1.5	40.5:55:4.5
18:79:3	15:82:3	37:56:7
17:77:6	14:79:7	33.5:53.5:13
17:74:9	12:79:9	N/A
15:70:15	13:74:13	23:52:25

1 as well as in Figure S3. An in-depth analysis of these results indicates that the composition of the precursor alloy is close to the elemental ratio in the input solution. The loading of Pt, which is essential for assessing the ORR activity, was evaluated by considering the EDX composition and the total electrochemical deposition charge. The EDX analysis suggests that some amount of Cu was retained after the oxidative stripping. This could be due to the pinning mobility of Pt which features much slower surface diffusion rates than Au does.[22,23]

The composition of the prepared catalysts was also determined using XPS (data summarized in Table S2 in the Supporting Information). Because of the fact that XPS is very surface sensitive (~5 nm), the composition from the XPS results reflects the surface elemental distribution, showing much less Cu (most of the Cu was buried underneath) than the EDX results (Table S2 in the Supporting Information). This provides indirect evidence to support the formation of a ligament-core (Cu) and shell (Pt and Au) structure. The valence states of Pt, Cu, and Au on the porous films were determined using XPS as shown in Figure 3. Figure 3a presents the Pt 4f spectra of the prepared porous films. The measured binding energies (BEs) of Pt $4f_{7/2}$ in the $Pt_{45}Cu_{55}$ (71.35 eV) and $Pt_{37}Cu_{56}Au_7$ (71.26 eV) porous films are slightly higher than that of pure Pt $4f_{7/2}$ (71.2 eV).[32,33] The XPS core level BE generally tracks the center of mass of the valence local density of states (LDOSs) in metals. For a more than half-filled band as is the case here and applying local charge neutrality, the increase in the BE, brought about by alloying Pt with the transition metal (Cu in the present case), should indicate an increase of the bandwidth of Pt.[20] This causes a Pt d-band center downshifting in comparison to monometallic Pt.[20,34] The doping with Au decreases the BE of the $Pt_{37}Cu_{56}Au_7$ porous film, indicating a slightly higher Pt d-band center in the porous film, compared with the $Pt_{45}Cu_{55}$ one. However, with an increase in the Au content, the BE of Pt $4f_{7/2}$ (70.96 eV) in $Pt_{23}Cu_{52}Au_{25}$ shifts negatively from the pure Pt $4f_{7/2}$ (71.2 eV). This suggests an upshift of the Pt d-band center. Figure 3b shows the core level Cu 2p XPS spectra. The BE of Cu $2p_{3/2}$ and Cu $2p_{1/2}$ features a slightly positive shift compared with the respective peaks of pure Cu reported before.[35] This would suggest a broadening of the Cu LDOS and, taken together with the Pt shifts, an increased bandwidth in the Pt−Cu system.[36] Figure 3c shows the XPS spectra of Au 4f, which are assigned to the BE of the Au $4f_{7/2}$ and Au $4f_{5/2}$ of pure Au.[37]

3.2. Electrochemical Performance of Prepared Catalysts. *3.2.1. Surface Area and Adsorption Properties.* The H UPD was used to probe the ECSA of Pt as shown in Figure 4a. The hydrogen adsorption and desorption areas in the potential region from −0.65 to −0.40 V (vs MSE) were used as a measure of the Pt area fraction on the catalyst's surface. From Figure 4a, it can be seen that the hydrogen adsorption and desorption areas increase with an increase of the Pt content in the porous films, as would be anticipated. However, the complex surface structure of these alloys could restrict the H adsorption on certain Pt sites,[38−41] generally leading to an underestimate of the Pt area when the H UPD method is used.

https://dx.doi.org/10.1021/acscatal.0c02690
ACS Catal. 2020, 10, 9967−9976

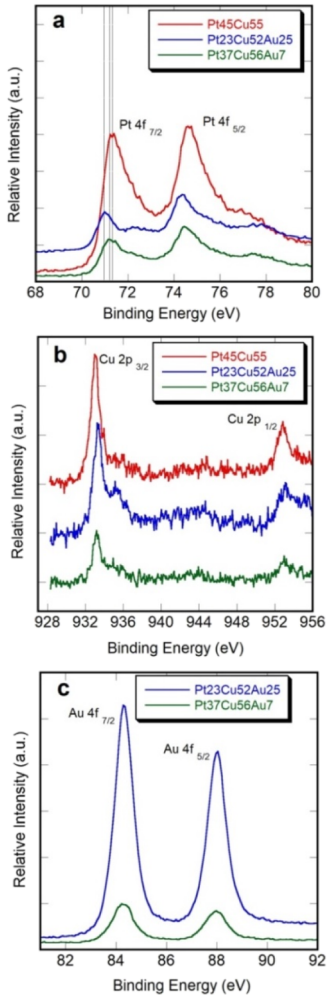

Figure 3. XPS spectra of different ratio Pt−Cu−Au porous films (a) Pt 4f; (b) Cu 2p; and (c) Au 4f.

Because CO adsorption is extremely weak on Au surfaces, the CO stripping method can be used to exclusively quantify the ECSA of Pt.[42] In such cases, it is important to confirm the ECSA by the CO stripping method.

The CO stripping method was utilized to probe, exclusively, the Pt surface area fraction in a more accurate and precise way. The Pt area was calculated by normalizing the CO stripping charge by 420 $\mu C/cm^2$, and the resulting number was further used for calculating the $ECSA_{(Pt)}$. The ECSAs of $Pt_{37}Cu_{56}Au_7$, $Pt_{23}Cu_{52}Au_{25}$, $Pt_{45}Cu_{55}$ porous films, and Pt/C (40 wt % Pt) (used as a reference catalyst) were thus calculated to be 47.08, 25.97, 45.81, and 53.50 m^2/g_{Pt}, respectively. The ECSA values indicate that the thin-film architectures developed in this work could provide higher surface area that leads more active sites for the ORR which makes the catalyst comparable to commercial 40 wt % Pt/C (~5 nm particle size). As seen in Figure 4b, the CO stripping peaks shift negatively from the $Pt_{37}Cu_{56}Au_7$ (at 0.782 V) porous film to the $Pt_{45}Cu_{55}$ (at 0.737 V) one, in comparison with the Pt/C (40 wt % Pt, at 0.791 V) catalyst.

The negative shift of the CO stripping peak indicates a weak bonding between CO and Pt sites, which is associated with a downshift of the d-band center.[15] This downshift of the Pt d-band center was also suggested in previous computational studies of the Pt−Cu alloy system.[20,43,44] It is worth emphasizing that doping with Au in small amounts (in the case of $Pt_{37}Cu_{56}Au_7$, red curve) results in a positive shift of the CO stripping peak, implying a stronger Pt−CO interaction compared with the case of the Au-free porous film ($Pt_{55}Cu_{45}$, green curve). This difference is most likely due to the fact that Au could upshift the d-band center of Pt,[44] increasing the adsorption energy of Pt−CO. The blue line in Figure 4b shows the CO stripping curve for a $Pt_{23}Cu_{52}Au_{25}$ porous film in which the Au content was higher. As expected, the CO stripping peak position was shifted to even more positive potentials, pointing toward an even stronger Pt−CO interaction.[44] In addition to the CO stripping peak position, the ratio of Q_{CO} to $2Q_H$, presented for all catalysts in Table 2, could also provide additional information about the surface structure.[45] Ideally, Q_{CO} should be equal to $2Q_H$,[27,29] which is the case for Pt/C (40% wt).[45] In the case of our thin-film catalysts, however, H adsorption could be suppressed by surface-segregated Au[39,41]

Table 2. Ratio between Q_{CO} and $2Q_H$ for Pt−Cu−Au Porous Films and Pt/C (40 wt % Pt)

catalysts	$Q_{CO}/2Q_H$
$Pt_{37}Cu_{56}Au_7$ porous film	1.61
$Pt_{23}Cu_{52}Au_{25}$ porous film	1.74
$Pt_{45}Cu_{55}$ porous film	1.49
Pt/C (40 wt % Pt)	1.15

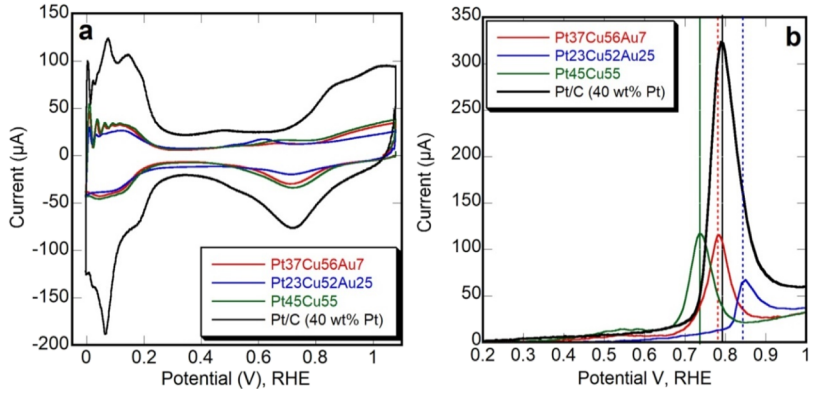

Figure 4. (a) H UPD curve on Pt/C (40 wt % Pt) and Pt−Cu−Au porous films with different compositions in 0.5 M H_2SO_4; scan rate 50 mV/s; (b) CO stripping (first sweep) on Pt/C (40 wt % Pt) and Pt−Cu−Au porous films with different compositions in 0.5 M H_2SO_4; scan rate 50 mV/s.

https://dx.doi.org/10.1021/acscatal.0c02690
ACS Catal. 2020, 10, 9967−9976

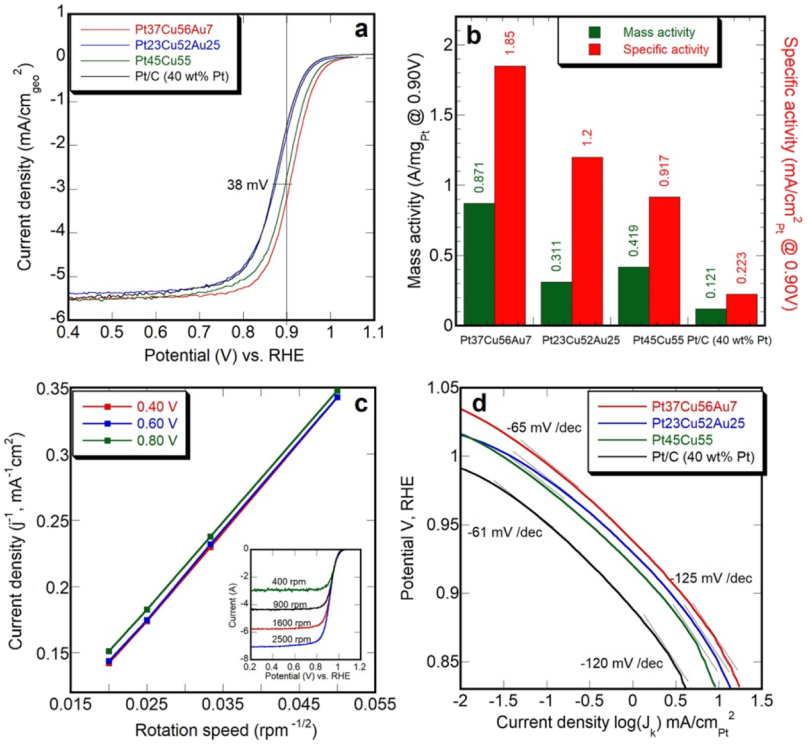

Figure 5. (a), ORR polarization curves of porous films with compositions $Pt_{37}Cu_{56}Au_7$, $Pt_{23}Cu_{52}Au_{25}$, and $Pt_{45}Cu_{55}$ along with commercial Pt/C (40 wt % Pt) under oxygen saturated 0.1 M KOH solution at a scan rate of 10 mV/s. Current density is normalized to the geometric area of the RDE (0.196 cm^2); (b) mass activity (left) and specific activity (right) of $Pt_{37}Cu_{56}Au_7$, $Pt_{23}Cu_{52}Au_{25}$, $Pt_{45}Cu_{55}$ porous films and commercial Pt/C (40 wt % Pt) at 0.90 V vs RHE; (c) K–L plots (j^{-1} vs $\omega^{-1/2}$) at different potentials. The inset shows ORR polarization curves of a $Pt_{37}Cu_{56}Au_7$ porous film at different rotation speeds; (d) natural log current density Tafel plot for $Pt_{37}Cu_{56}Au_7$, $Pt_{23}Cu_{52}Au_{25}$, $Pt_{45}Cu_{55}$ porous films, and commercial Pt/C (40 wt % Pt).

and/or the strain effect of the Pt-skin structure.[38,40] Previous studies[45] indicate that a Pt-skin structure possesses a $Q_{CO}/2Q_H$ ratio of ~1.50. The $Q_{CO}/2Q_H$ ratio for the $Pt_{45}Cu_{55}$ porous film was 1.49, suggesting a Pt-skin structure. With doping of Au, the ratio keeps increasing (e.g. 1.61 and 1.74), indicating that the Au component, segregated on the catalyst surface, suppresses the adsorption of H on Pt sites.[39,41]

3.2.2. Catalyst Activity, Overall Performance, and the ORR Mechanism. Figure 5a displays the LSV curves of $Pt_{37}Cu_{56}Au_7$, $Pt_{23}Cu_{52}Au_{25}$, $Pt_{45}Cu_{55}$ porous films, and commercial Pt/C (40 wt % Pt) under an oxygen-saturated environment at a scan rate of 10 mV/s and a rotation rate of 1,600 rpm. The half-wave potential of the $Pt_{37}Cu_{56}Au_7$ porous film (0.909 V) is 38 mV positive of the commercial Pt/C reference sample (0.871 V), revealing its superior electrocatalytic activity toward the ORR in alkaline solution. While the $Pt_{45}Cu_{55}$ porous film was less active than the $Pt_{37}Cu_{56}Au_7$ porous film, its half-wave potential (0.896 V) was still shifted 25 mV positive of the commercial Pt/C (40 wt % Pt) sample. The specific activity (normalized to the Pt area obtained from CO stripping) and the mass activity (normalized to the mass of Pt) which are summarized in Figure 5b for these thin-film catalysts were measured at 0.90 V (vs RHE) and calculated via the K–L equation (eq 2) before *iR* correction. The catalytic mass activities, after *iR* correction, are summarized in Table S3 in the Supporting Information. The mass activity and specific activity of the $Pt_{37}Cu_{56}Au_7$ porous film were 7.2× (8.7×, *iR* corrected) and 8.15× (11.3×, *iR* corrected) higher than those of the commercial Pt/C (40 wt % Pt), respectively. This corroborates the excellent activity of these thin-film catalysts toward the ORR. Because Au could also contribute to the ORR performance in alkaline media,[6,10] the Pt- and Au-based total mass was also considered in the mass activity calculation (Table S3 in the Supporting Information). Even when considering the combined Pt + Au mass in the calculation, the $Pt_{37}Cu_{56}Au_7$ porous film still showed a 6.3× higher mass activity than the commercial Pt/C (40 wt % Pt).

It is well-known that the electronic structure of Pt can be tuned by extra-filling its d-orbital via electron transfer from other (usually first row) transition metals (Cu, Co, Ni, Fe, etc.), resulting in a downshifting of the Pt d-band center.[15,20,43] The alloy porous structure could be formed through a dealloying process with a mostly Cu-containing core and a Pt(Au)-rich shell ligament structure.[15,46] The ligand effect[11] of Cu could further promote the Pt d-band center downshift, which is corroborated by the positive shift in the BE of Pt in its XPS spectra (Figure 3a). In this case, the catalytic activity could be improved by weakening the binding between Pt and oxygenated species.[19] Furthermore, the Sabatier principle[47,48] predicts that the ORR should reach the maximum activity when the electrocatalyst binds oxygenated species and oxygen with moderate (ostensibly optimal) strength.[49] According to the CO stripping (Figure 4b) and XPS results (Figure 3a), the $Pt_{45}Cu_{55}$ porous film possesses the lowest Pt d-band center, indicating that the BE between the oxygenated intermediates and the catalyst surface may be too weak to keep the necessary oxygen adsorption. On the other hand, the $Pt_{23}Cu_{52}Au_{25}$ porous film exhibited the highest upshift of the Pt d-band center among all the studied samples. This would give rise to a very strong binding affinity between the oxygenated

https://dx.doi.org/10.1021/acscatal.0c02690
ACS Catal. 2020, 10, 9967–9976

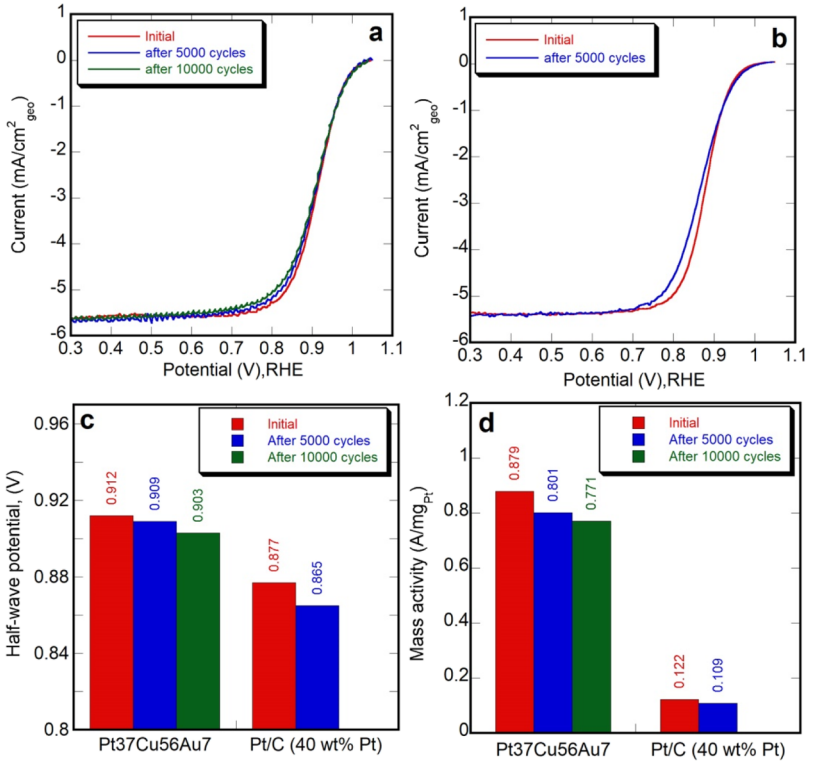

Figure 6. ORR polarization curves, half-wave potential change, and mass activity change measured under oxygen saturated 0.1 M KOH solution at a scan rate of 10 mV/s (a) ORR polarization curves of a $Pt_{37}Cu_{56}Au_7$ porous film at the initial test and after 5,000 ADT cycles and 10,000 ADT cycles; (b) ORR polarization curves of commercial Pt/C (40 wt % Pt) at the initial test and after 5,000 ADT cycles; (c) half-wave potential change for the $Pt_{37}Cu_{56}Au_7$ porous film and commercial Pt/C (40 wt % Pt) after ADT; (d) mass activity change of a $Pt_{37}Cu_{56}Au_7$ porous film and Pt/C (40 wt % Pt) after ADT.

intermediates and the Pt active sites. In such a case, the accumulation of oxygenated species would hinder the rate of desorption of ORR product species and thereby result in a sluggish overall ORR. Another factor that could give rise to the lower activity of the $Pt_{23}Cu_{52}Au_{25}$ porous film could be the higher Au content that effectively reduces the number of active sites for the ORR. However, this effect appears to be secondary because if it were the main one, the specific/mass activity (vs Pt) should remain constant. Trace amounts of Au (e.g. $Pt_{37}Cu_{56}Au_7$ porous film) could tune the Pt d-band center position, as illustrated by XPS and CO stripping data, optimizing the ORR activity as suggested by the volcano diagram presented in Figure S4. In addition, the synergistic effect between Pt and Au could also enhance the ORR performance. This could take place by the chemisorbed OH^- on the Au surface acting as a precursor for promoting either the molecular oxygen breakdown or a reaction intermediate formation.[17,46] In order to investigate the role of Au in the ORR, Au was deposited in small clusters on a flat Pt electrode by a pulse deposition procedure. Its H UPD curve (Figure S5a) showed a decrease (anticipated) of the H adsorption/desorption area of the Au-decorated Pt electrode. Because H adsorbs only on the Pt surface, the above-mentioned H UPD would be consistent with the presence of partial Au coverage on the Pt electrode surface. The LSV (Figure S5b) shows a slightly positively shifted (~6 mV) half-wave potential for the Au doped Pt electrode, implying a generally better ORR performance. This experiment shows the impact of the synergistic effect(s) between Au and Pt on the ORR activity promotion in alkaline media.

The number of electrons transferred (n) for the $Pt_{37}Cu_{56}Au_7$ porous film (the most active sample) as the ORR catalyst was calculated based on the K–L equation as described in eq 3 using the slopes of the K–L plots in Figure 5c. The calculated n values at potentials of 0.40, 0.60,, and 0.80 V were 3.93, 3.92, and 3.86, respectively. These results suggest a dominant four-electron pathway toward the ORR. Each Tafel plot for $Pt_{37}Cu_{56}Au_7$, $Pt_{23}Cu_{52}Au_{25}$, $Pt_{45}Cu_{55}$ porous films, and commercial Pt/C (40 wt % Pt) featured two linear regions with slopes of around −120 mV/dec at high overpotentials and around −60 mV/dec at low overpotentials (Figure 5d). The slope shifts from an initial value of −60 to −120 mV/dec, indicating a mechanism that is limited by the initial reduction of O_2.[50,51] These Tafel slopes are similar to those previously reported for Pt catalysts,[51,52] suggesting that the reaction mechanism on these thin-film alloy catalysts is the same as that of Pt catalysts.

3.2.3. Catalyst Durability. The durability of a catalyst can play an important, even dominant, role in practical applications. To assess the durability of the thin-film catalysts developed in this work, ADTs of up to 10,000 potential cycles were conducted in an O_2-saturated 0.1M KOH solution over the potential region between 0.6 and 1.0 V at a scan rate of 100 mV/s. Figure 6a,b shows the LSV curves before and after ADTs to assess the performance change of a $Pt_{37}Cu_{56}Au_7$ porous film and commercial Pt/C (40 wt % Pt). All the profiles exhibited a negative shift after a long-term ADT, indicating a trend toward a lower catalytic activity. Figure 6c compares the results of half-wave potential measurements of a $Pt_{37}Cu_{56}Au_7$ porous film versus Pt/C (40 wt % Pt), showing only a 9 mV negative shift after 10,000 ADT potential cycles (3 mV after

https://dx.doi.org/10.1021/acscatal.0c02690
ACS Catal. 2020, 10, 9967–9976

5000 cycles) for the ternary catalyst and a substantially more significant shift of 12 mV for Pt/C (40 wt % Pt) after 5,000 ADT cycles. In terms of the mass activity comparison presented in Figure 6d, the $Pt_{37}Cu_{56}Au_7$ porous film exhibited a ~8.9% decrease after 5,000 ADT cycles, whereas Pt/C (40 wt % Pt) dropped by about 10.6% after the same testing routine was applied. Furthermore, the mass activity of $Pt_{37}Cu_{56}Au_7$ porous film after 10,000 ADT cycles remained around 6.3-times higher than the initial activity of the commercial Pt/C (40 wt % Pt). Figure S6 in the Supporting Information also presents the durability assessment of a binary $Pt_{45}Cu_{55}$ porous film. It can be seen that the half-wave potential exhibited a negative shift of 14 mV after 10,000 ADT cycles, suggesting that the durability of binary $Pt_{45}Cu_{55}$ is slightly worse than that of the $Pt_{37}Cu_{56}Au_7$ porous film. This may be caused by the Au doping in $Pt_{37}Cu_{56}Au_7$ that could stabilize the surface and potentially hinder the oxidation of Pt.[53] In an effort to identify the origin of the catalytic activity decrease after the ADT, a SEM−EDX characterization was carried out to probe the compositional changes before and after 5,000 ADT cycles for the $Pt_{37}Cu_{56}Au_7$ porous film (Figure S7). Interestingly, and somewhat surprisingly, these measurements did not show any major changes in the composition with the ADT progress, except for a 0.5% decrease in the Cu content after the ADT. In fact, a reported thermodynamic study indicated that Au is stable in alkaline solution, and Pt could form in a stable oxidation state (no dissolved species),[53] which is consistent with our EDX results. Based on the EDX evaluation and previous studies consisting of noble metal electrochemical dissolution in alkaline media and the compositional change of Cu−Pt nanocages,[54] we hypothesize that the oxidation of catalytically active sites (mostly Pt sites) could be the reason of for the ORR activity decrease in the $Pt_{37}Cu_{56}Au_7$ thin-film catalyst, although this degradation is minor.

4. CONCLUSIONS

In summary, we have presented a facile synthesis protocol of Pt−Cu−Au porous films through an electrochemical deposition−stripping approach. Among the tested thin-film catalysts, the $Pt_{37}Cu_{56}Au_7$ alloy one exhibited 7.20× and 8.15× higher mass and specific activities than those of Pt/C (40 wt % Pt), respectively. In addition to the excellent catalytic performance, the $Pt_{37}Cu_{56}Au_7$ porous film also exhibited promising durability as manifested by only a 9 mV negative shift in the half-wave potential after 10,000 potential cycles of the ADT. Thus, based on our study, the $Pt_{37}Cu_{56}Au_7$ porous film appears to be the most promising thin-film anodic catalyst in AFCs. Our preliminary mechanistic studies indicate that the down-shift of the Pt d-band center could arise as a result of the ligand effect and strain effect of underneath Cu in the ligament structure. Moreover, the synergistic effect between Au and Pt could also facilitate the ORR in alkaline media. The catalytic activity and the fraction of Au doping exhibits a volcano-shaped relationship. The results presented in this study bridge the ORR activity with electronic properties, composition, and microstructure in a way that could provide informative guidance for future electrocatalysts design and synthesis.

■ ASSOCIATED CONTENT

Supporting Information

The Supporting Information is available free of charge at https://pubs.acs.org/doi/10.1021/acscatal.0c02690.

Results of morphology (SEM) and surface area characterization (H UPD); composition assay before and after catalytic testing (EDS); activity and durability characterization (RDE testing); and catalytic performance without *iR* compensation (RDE testing) (PDF)

■ AUTHOR INFORMATION

Corresponding Authors

Nikolay Dimitrov − *Department of Chemistry, State University of New York at Binghamton, Binghamton, New York 13902, United States;* orcid.org/0000-0003-1787-4575; Phone: +1 (607) 777-4271; Email: dimitrov@binghamton.edu; Fax: +1 (607) 777-4478

Jiye Fang − *Department of Chemistry, State University of New York at Binghamton, Binghamton, New York 13902, United States*; Phone: +1 (607) 777 3752; Email: jfang@binghamton.edu; Fax: +1 (425) 988-1050

Authors

Yunxiang Xie − *Department of Chemistry, State University of New York at Binghamton, Binghamton, New York 13902, United States*

Yao Yang − *Department of Chemistry and Chemical Biology, Cornell University, Ithaca, New York 14853, United States;* orcid.org/0000-0003-0321-3792

David A. Muller − *School of Applied and Engineering Physics, Cornell University, Ithaca, New York 14853, United States*

Héctor D. Abruña − *Department of Chemistry and Chemical Biology, Cornell University, Ithaca, New York 14853, United States;* orcid.org/0000-0002-3948-356X

Complete contact information is available at: https://pubs.acs.org/10.1021/acscatal.0c02690

Notes

The authors declare no competing financial interest.

■ ACKNOWLEDGMENTS

This work was primarily supported by the Center for Alkaline-Based Energy Solutions, an Energy Frontier Research Center program supported by the US Department of Energy, under Grant DE-SC0019445. The CO-stripping characterizations were supported by the National Science Foundation (DMR 1808383), SEM−EDX measurements were partially supported by S3IP, State University of New York at Binghamton, and STEM EDX elemental mapping work was carried out using TEM facilities at the Cornell Center for Materials Research (CCMR) which are supported through the National Science Foundation Materials Research Science and Engineering Center program (DMR-1719875). We thank Anju Sharma for her help in XPS experiments. We also acknowledge Can Li and Yiliang Luan for their support of the Pt/C electrode preparation and the facilitation provided for the CO-stripping measurement. Y.X. gratefully acknowledges his partial financial support through ACS PRF (58196-ND10).

■ REFERENCES

(1) Uzunoglu, M.; Alam, M. S. *Power Electronics Handbook*; Rashid, M. H., Ed.; Elsevier, 2018; pp 1091−1112.

(2) Emadi, A.; Ehsani, M.; Miller, J. M. *Vehicular Electric Power Systems: Land, Sea, Air, and Space Vehicles*; Taylor & Francis Group, 2003; pp 242−290.

(3) Ramaswamy, N.; Mukerjee, S. Fundamental mechanistic understanding of electrocatalysis of oxygen reduction on Pt and

non-Pt surfaces: acid versus alkaline media. *Adv. Phys. Chem.* **2012**, *2012*, 1−17.
(4) Ge, X.; Sumboja, A.; Wuu, D.; An, T.; Li, B.; Goh, F. W. T.; Hor, T. S. A.; Zong, Y.; Liu, Z. Oxygen reduction in alkaline media: from mechanisms to recent advances of catalysts. *ACS Catal.* **2015**, *5*, 4643−4667.
(5) Debe, M. K. Electrocatalyst approaches and challenges for automotive fuel cells. *Nature* **2012**, *486*, 43−51.
(6) Schmidt, T. J.; Stamenkovic, V.; Arenz, M.; Markovic, N. M.; Ross, P. N., Jr. Oxygen electrocatalysis in alkaline electrolyte: Pt (hkl), Au (hkl) and the effect of Pd-modification. *Electrochim. Acta* **2002**, *47*, 3765−3776.
(7) Blizanac, B. B.; Ross, P. N.; Marković, N. M. Oxygen Reduction on Silver Low-Index Single-Crystal Surfaces in Alkaline Solution: Rotating Ring DiskAg (h kl) Studies. *J. Phys. Chem. B* **2006**, *110*, 4735−4741.
(8) Srejic, I.; Rakocevic, Z.; Nenadovic, M.; Strbac, S. Oxygen reduction on polycrystalline palladium in acid and alkaline solutions: topographical and chemical Pd surface changes. *Electrochim. Acta* **2015**, *169*, 22−31.
(9) Adžić, R. R.; Strbac, S.; Anastasijević, N. Electrocatalysis of oxygen on single crystal gold electrodes. *Mater. Chem. Phys.* **1989**, *22*, 349−375.
(10) Quaino, P.; Luque, N. B.; Nazmutdinov, R.; Santos, E.; Schmickler, W. Why is gold such a good catalyst for oxygen reduction in alkaline media? *Angew. Chem., Int. Ed.* **2012**, *51*, 12997−13000.
(11) Jensen, K. D.; Tymoczko, J.; Rossmeisl, J.; Bandarenka, A. S.; Chorkendorff, I.; Escudero-Escribano, M.; Stephens, I. E. L. Elucidation of the oxygen reduction volcano in alkaline media using a copper−platinum (111) alloy. *Angew. Chem., Int. Ed.* **2018**, *57*, 2800−2805.
(12) Zhao, Y.; Wu, Y.; Liu, J.; Wang, F. Dependent Relationship between Quantitative Lattice Contraction and Enhanced Oxygen Reduction Activity over Pt−Cu Alloy Catalysts. *ACS Appl. Mater. Interfaces* **2017**, *9*, 35740−35748.
(13) Wang, S.; Xiong, L.; Bi, J.; Zhang, X.; Yang, G.; Yang, S. Structural and Electronic Stabilization of PtNi Concave Octahedral Nanoparticles by P Doping for Oxygen Reduction Reaction in Alkaline Electrolytes. *ACS Appl. Mater. Interfaces* **2018**, *10*, 27009−27018.
(14) Kitchin, J. R.; Nørskov, J. K.; Barteau, M. A.; Chen, J. Role of strain and ligand effects in the modification of the electronic and chemical properties of bimetallic surfaces. *Phys. Rev. Lett.* **2004**, *93*, 156801.
(15) Bligaard, T.; Nørskov, J. K. Ligand effects in heterogeneous catalysis and electrochemistry. *Electrochim. Acta* **2007**, *52*, 5512−5516.
(16) Gong, H.; Cao, X.; Mendes, R. G.; Rummeli, M. H.; Zhang, J.; Yang, R. Self-Supported PtAuCu@ Cu2O/Pt Hybrid Nanobranch as a Robust Electrocatalyst for the Oxygen Reduction Reaction. *ChemElectroChem* **2017**, *4*, 1554−1559.
(17) Feng, J.-J.; He, L.-L.; Fang, R.; Wang, Q.-L.; Yuan, J.; Wang, A.-J. Bimetallic PtAu superlattice arrays: highly electroactive and durable catalyst for oxygen reduction and methanol oxidation reactions. *J. Power Sources* **2016**, *330*, 140−148.
(18) Wang, A.-J.; Zhang, X.-F.; Jiang, L.-Y.; Zhang, L.; Feng, J.-J. Bimetallic Alloyed PtCu Nanocubic Frames with Three-Dimensional Molecular Accessible Surfaces for Boosting Oxygen Reduction and Glycerol Oxidation Reactions. *ChemCatChem* **2018**, *10*, 3319−3326.
(19) Stamenkovic, V.; Mun, B. S.; Mayrhofer, K. J. J.; Ross, P. N.; Markovic, N. M.; Rossmeisl, J.; Greeley, J.; Nørskov, J. K. Changing the activity of electrocatalysts for oxygen reduction by tuning the surface electronic structure. *Angew. Chem., Int. Ed.* **2006**, *45*, 2897−2901.
(20) Ruban, A.; Hammer, B.; Stoltze, P.; Skriver, H. L.; Nørskov, J. K. Surface electronic structure and reactivity of transition and noble metals. *J. Mol. Catal. A: Chem.* **1997**, *115*, 421−429.
(21) Xie, Y.; Dimitrov, N. Ultralow Pt loading nanoporous Au-Cu-Pt thin film as highly active and durable catalyst for formic acid oxidation. *Appl. Catal., B* **2020**, *263*, 118366.
(22) Snyder, J.; Asanithi, P.; Dalton, A. B.; Erlebacher, J. Stabilized nanoporous metals by dealloying ternary alloy precursors. *Adv. Mater.* **2008**, *20*, 4883−4886.
(23) El-Zoka, A. A.; Langelier, B.; Korinek, A.; Botton, G. A.; Newman, R. C. Nanoscale mechanism of the stabilization of nanoporous gold by alloyed platinum. *Nanoscale* **2018**, *10*, 4904−4912.
(24) Xie, Y.; Li, C.; Razek, S. A.; Fang, J.; Dimitrov, N. Synthesis of Nanoporous Au− Cu− Pt Alloy as a Superior Catalyst for the Methanol Oxidation Reaction. *ChemElectroChem* **2020**, *7*, 569−580.
(25) Ambrozik, S.; Mitchell, C.; Dimitrov, N. The spontaneous deposition of Au on Pt (111) and polycrystalline Pt. *J. Electrochem. Soc.* **2016**, *163*, D3001−D3007.
(26) Trasatti, S.; Petrii, O. A. Real surface area measurements in electrochemistry. *J. Electroanal. Chem.* **1992**, *327*, 353−376.
(27) Chen, Q.-S.; Solla-Gullón, J.; Sun, S.-G.; Feliu, J. M. The potential of zero total charge of Pt nanoparticles and polycrystalline electrodes with different surface structure: The role of anion adsorption in fundamental electrocatalysis. *Electrochim. Acta* **2010**, *55*, 7982−7994.
(28) Clavilier, J.; Albalat, R.; Gomez, R.; Orts, J. M.; Feliu, J. M.; Aldaz, A. Study of the charge displacement at constant potential during CO adsorption on Pt (110) and Pt (111) electrodes in contact with a perchloric acid solution. *J. Electroanal. Chem.* **1992**, *330*, 489−497.
(29) Vidaković, T.; Christov, M.; Sundmacher, K. The use of CO stripping for in situ fuel cell catalyst characterization. *Electrochim. Acta* **2007**, *52*, 5606−5613.
(30) Koutecky, J.; Levich, B. The application of the rotating disc electrode to studies of kinetic and catalytic processes. *Zh. Fiz. Khim.* **1958**, *32*, 1565−1575.
(31) Xia, T.; Liu, J.; Wang, S.; Wang, C.; Sun, Y.; Gu, L.; Wang, R. Enhanced catalytic activities of NiPt truncated octahedral nanoparticles toward ethylene glycol oxidation and oxygen reduction in alkaline electrolyte. *ACS Appl. Mater. Interfaces* **2016**, *8*, 10841−10849.
(32) Schneider, W.-D.; Laubschat, C. Actinide—noble-metal systems: An x-ray-photoelectron-spectroscopy study of thorium-platinum, uranium-platinum, and uranium-gold intermetallics. *Phys. Rev. B: Condens. Matter Mater. Phys.* **1981**, *23*, 997.
(33) Wagner, C. D. Chemical Shifts of Auger Lines, and the Auger Parameter. *Faraday Discuss. Chem. Soc.* **1975**, *60*, 291−300.
(34) Corcoran, C. J.; Tavassol, H.; Rigsby, M. A.; Bagus, P. S.; Wieckowski, A. Application of XPS to study electrocatalysts for fuel cells. *J. Power Sources* **2010**, *195*, 7856−7879.
(35) Kowalczyk, S. P.; Pollak, R. A.; McFeely, F. R.; Ley, L.; Shirley, D. A. L 2, 3 M 45 M 45 auger spectra of metallic copper and zinc: theory and experiment. *Phys. Rev. B: Solid State* **1973**, *8*, 2387.
(36) Muller, D. A. Why changes in bond lengths and cohesion lead to core-levels in metals, and consequences for the spatial difference method. *Ultramicroscopy* **1999**, *78*, 163−174.
(37) Mansour, A. N. Gold Mg K α XPS spectra from the physical electronics model 5400 spectrometer. *Surf. Sci. Spectra* **1994**, *3*, 197−201.
(38) Chen, S.; Sheng, W.; Yabuuchi, N.; Ferreira, P. J.; Allard, L. F.; Shao-Horn, Y. Origin of oxygen reduction reaction activity on "Pt3Co" nanoparticles: atomically resolved chemical compositions and structures. *J. Phys. Chem. C* **2008**, *113*, 1109−1125.
(39) Bergbreiter, A.; Alves, O. B.; Hoster, H. E. Entropy Effects in Atom Distribution and Electrochemical Properties of AuxPt1− x/Pt (111) Surface Alloys. *ChemPhysChem* **2010**, *11*, 1505−1512.
(40) Wang, C.; Van Der Vliet, D.; More, K. L.; Zaluzec, N. J.; Peng, S.; Sun, S.; Daimon, H.; Wang, G.; Greeley, J.; Pearson, J. Multimetallic Au/FePt3 nanoparticles as highly durable electrocatalyst. *Nano Lett.* **2010**, *11*, 919−926.

https://dx.doi.org/10.1021/acscatal.0c02690
ACS Catal. 2020, 10, 9967−9976

(41) Suntivich, J.; Xu, Z.; Carlton, C. E.; Kim, J.; Han, B.; Lee, S. W.; Bonnet, N.; Marzari, N.; Allard, L. F.; Gasteiger, H. A.; Hamad-Schifferli, K.; Shao-Horn, Y. Surface composition tuning of Au−Pt bimetallic nanoparticles for enhanced carbon monoxide and methanol electro-oxidation. *J. Am. Chem. Soc.* **2013**, *135*, 7985−7991.
(42) Chang, S. C.; Hamelin, A.; Weaver, M. J. Dependence of the electrooxidation rates of carbon monoxide at gold on the surface crystallographic orientation: A combined kinetic-surface infrared spectroscopic study. *J. Phys. Chem.* **1991**, *95*, 5560−5567.
(43) Hammer, B.; Nørskov, J. K. *Advances in Catalysis*; Elsevier, 2000; Vol. *45*, pp 71−129.
(44) Demirci, U. B. Theoretical means for searching bimetallic alloys as anode electrocatalysts for direct liquid-feed fuel cells. *J. Power Sources* **2007**, *173*, 11−18.
(45) van der Vliet, D. F.; Wang, C.; Li, D.; Paulikas, A. P.; Greeley, J.; Rankin, R. B.; Strmcnik, D.; Tripkovic, D.; Markovic, N. M.; Stamenkovic, V. R. Unique electrochemical adsorption properties of Pt-Skin Surfaces. *Angew. Chem., Int. Ed.* **2012**, *51*, 3139−3142.
(46) Štrbac, S.; Adžić, R. The influence of OH− chemisorption on the catalytic properties of gold single crystal surfaces for oxygen reduction in alkaline solutions. *J. Electroanal. Chem.* **1996**, *403*, 169−181.
(47) Medford, A. J.; Vojvodic, A.; Hummelshøj, J. S.; Voss, J.; Abild-Pedersen, F.; Studt, F.; Bligaard, T.; Nilsson, A.; Nørskov, J. K. From the Sabatier principle to a predictive theory of transition-metal heterogeneous catalysis. *J. Catal.* **2015**, *328*, 36−42.
(48) Sabatier, P. *La catalyse en chimie organique*; Nouveau Monde éditions Hachette Livre-BNF, 2014.
(49) Xia, W.; Mahmood, A.; Liang, Z.; Zou, R.; Guo, S. Earth-abundant nanomaterials for oxygen reduction. *Angew. Chem., Int. Ed.* **2016**, *55*, 2650−2676.
(50) Zhang, J. *PEM Fuel Cell Electrocatalysts and Catalyst Layers: Fundamentals and Applications*; Springer Science & Business Media, 2008.
(51) Holewinski, A.; Linic, S. Elementary mechanisms in electrocatalysis: revisiting the ORR Tafel slope. *J. Electrochem. Soc.* **2012**, *159*, H864.
(52) Lu, Y.; Jiang, Y.; Gao, X.; Wang, X.; Chen, W. Strongly coupled Pd nanotetrahedron/tungsten oxide nanosheet hybrids with enhanced catalytic activity and stability as oxygen reduction electrocatalysts. *J. Am. Chem. Soc.* **2014**, *136*, 11687−11697.
(53) Schalenbach, M.; Kasian, O.; Ledendecker, M.; Speck, F. D.; Mingers, A. M.; Mayrhofer, K. J. J.; Cherevko, S. The electrochemical dissolution of noble metals in alkaline media. *Electrocatal* **2018**, *9*, 153−161.
(54) Dhavale, V. M.; Kurungot, S. Cu−Pt nanocage with 3-D electrocatalytic surface as an efficient oxygen reduction electrocatalyst for a primary Zn−air battery. *ACS Catal.* **2015**, *5*, 1445−1452.

https://dx.doi.org/10.1021/acscatal.0c02690
ACS Catal. 2020, 10, 9967−9976